Observation of photovoltaic effect within locally doped silicon nanojunctions using conductive probe AFM

R. Khoury, J Alvarez, T. Ohashi, I. Martín, P. Ortega, G. Lopez, C. Jin, Z. Li, - Rusli, P. Bulkin, et al.

Observation of photovoltaic effect within locally doped silicon nanojunctions using conductive probe AFM

R. Khoury [a], J. Alvarez [b,c], T. Ohashi [b,c], I. Martín [d], P. Ortega [d], G. López [d], C. Jin [d], Z. Li [e], Rusli [e], P. Bulkin [a], E.V. Johnson [a,*]

[a] LPICM, CNRS, Ecole Polytechnique, Institut Polytechnique de Paris, 91128, Palaiseau, France
[b] Université Paris-Saclay, CentraleSupélec, CNRS, Laboratoire de Génie Electrique et Electronique de Paris, 91192, Gif-sur-Yvette, France
[c] Sorbonne Université, CNRS, Laboratoire de Génie Electrique et Electronique de Paris, 75252, Paris, France
[d] Departament d'Enginyeria Electrònica, Universitat Politècnica de Catalunya, Gran Capità s/n, Mòdul C4, 08034, Barcelona, Spain
[e] NOVITAS, Nanoelectronics Centre of Excellence, School of Electrical and Electronic Engineering, Nanyang Technological University, 50 Nanyang Avenue, 639798, Singapore

ABSTRACT

Localized p-doped nanojunctions (200–300 nm in diameter) were formed in n-type crystalline silicon substrates and were characterized using scanning electron microscopy (SEM) and conductive-probe atomic force microscopy (C-AFM). Localized doping was performed by diffusion through sub-micron sized holes in a silicon-oxide mask defined using self-organized polystyrene nanoparticles. After oxide removal, a significant brightness contrast in the SEM top and side view images strongly suggested the successful local doping of these areas. Furthermore, local current-voltage measurements performed by C-AFM revealed an open circuit voltage and a short-circuit current only in the areas defined as nanojunctions. This photovoltaic effect is driven by the laser used to control cantilever deflection in the AFM.

1. INTRODUCTION

The passivated emitter and rear cell (PERC) is an attractive structure for cost-effective, high-efficiency photovoltaic (PV) devices. The main feature of this solar cell design is a rear surface partially contacted by periodical openings in the dielectric film that provides surface passivation. As a result, lower effective rear surface recombination velocity ($S_{\mathrm{eff,\,rear}}$) values are observed compared to the classical aluminum back-surface field (Al-BSF) design, as well as a higher rear internal reflectance leading to improved short-circuit current (I_{SC}) and open-circuit voltage (V_{OC}) in the resulting finished devices.

This type of solar cell was developed by Blakers et al., in 1988, and using thermally grown silicon oxide as a passivating layer, they demonstrated a record (at the time) efficiency for silicon cells of 22.8% [1]. In order to passivate the contacts, a local BSF at the contacted regions was later introduced. This passivated emitter rear locally diffused cell (PERL) was demonstrated by the University of New South Wales in Australia in 1999 to be capable of a new record efficiency of 25% [2]. Although such designs were unveiled in the 90's, it is only in recent years that PERC/L solar cells have been introduced into the PV market for p-type substrates. The original designs used photolithography to pattern the contacts and thermal oxide for passivation, and only the subsequent development of aluminum oxide/silicon nitride passivation and laser ablation/doping has led to the required considerable reduction of the fabrication costs [3]. In recent years, the research focus for PERC devices has been improving efficiency at industrial scales and throughputs, while maintaining the reduced costs necessary to remain competitive [4,5].

When the rear contact of a solar cell is defined as a pattern of points, as in a PERC device, an optimization must be made to maximize the conversion efficiency; a greater contacted area fraction (f_c), leads to lower ohmic losses (and a greater Fill Factor, *FF*), but a higher surface recombination rate (and lower V_{OC} and I_{sc}). Examples of such optimization can be found in the literature [6,7]. Due to the characteristics of the conventional, laser-based procedure to locally open the contacts in the passivation layer, typical dimensions for the contacts are in the range of tens of microns while optimized f_c values are well below 10%. As a consequence, the distance between neighboring contacts (or pitch, p) is on the order of hundreds of microns, introducing a significant series resistance.

In previous work, we have explored the electrical benefits of using contact openings with sizes in the range of 1 μm [8]. We have demonstrated that at constant f_c, lower ohmic losses can be obtained with smaller contacts due to the shorter pitches. This advantage for small contact openings can be also exploited by using longer pitch values with reasonable ohmic losses resulting in less of the surface being covered by contacts. The benefit of this will clearly depend on the passivation quality of the contacts, quantified by their contact surface recom-

bination velocities (S_{cont}). Indeed, as S_{cont} takes on increasing values from 10^2-10^5 cm/s, PC-1D simulation results indicate that smaller contacts result in a possible optimized efficiency gain of almost 1% absolute.

Following the advantages pointed out by simulations, in this work we demonstrate the formation of an array of locally p-doped nanojunctions in n-type crystalline silicon (c-Si) wafers that could be applied to the rear surface of a solar cell. The array of regularly distributed contacts is formed using nanoscale holes in an oxide diffusion mask, created through a multi-step process employing self-organized polystyrene (PS) nanoparticles (NPs). The use of spun-on, randomly distributed PS spheres as a mask to make point contacts has been previously demonstrated for PERC cells, but with sphere sizes comparable to those of laser openings (40 μm) [9]. In this work, after oxide removal, the presence of localized doping at the nanometer scale is examined using scanning electron microscopy (SEM) and conductive probe atomic force microscopy (C-AFM). Interest in the latter technique, also called CP-AFM, has grown since the 1990s due to its ease of use, enabling the investigation of a wide range of materials in different forms (thin films, bulk, nanostructured …) and over a wide range of electrical conductivities (metals, insulators and semiconductors) [10–15]. Semiconductor nanostructures and devices have also greatly benefited from this technique to probe their electrical properties and heterogeneities, leakage current paths, carrier transport mechanisms, as well as photoelectric properties [16–25]. In particular, in the field of PV, local scale C-AFM investigations (in dark and illuminated conditions) have demonstrated added value in understanding charge transport and in improving the performance of the final device. Numerous C-AFM studies have been carried out on different solar cell configurations (planar, nanowires, cross-section, …) and in particular, on the layers or structures of which they are composed [26–32]. In this work, the C-AFM method will be used to directly probe the photovoltaic properties of nanojunctions formed in a c-Si wafer.

2. Materials and methods

2.1. Chemicals and materials

The PS NPs used in this work had nominal diameters of 607±15 nm and 784±15 nm, and were obtained as an aqueous suspension of 5 wt % (from microParticles GmbH). For simplicity, these will be referred to as 600 nm and 800 nm NPs. The suspension was first diluted by mixing it with an equal volume of methanol as the spreading agent. Then, a 5-min ultrasound bath at low power was performed to prevent NP agglomeration and give a more uniform dispersion of the NPs in the suspension. The c-Si wafers (100) with a 120 nm or 240 nm thick passivation layer of thermally grown silicon oxide were cleaned with acetone, isopropanol (IPA) and de-ionized (DI) water. The wafers were exposed to a UV ozone treatment for 10 min to temporarily obtain a highly hydrophilic surface prior to use.

2.2. NP monolayer formation and etching

In this work, the floating-transfer technique was used to deposit a compact monolayer of PS NPs on n-type c-Si substrates, as described in previous publications [33,34]. This technique involves forming a monolayer of self-assembled, hexagonally close-packed PS NPs on the surface of a water-filled Petri dish, then slowly lifting a pre-immersed c-Si substrate out of the water, so that the PS NPs monolayer is transferred onto the substrate surface.

However, the compact monolayer of NPs produced by the floating-transfer technique is not suitable generating a mask for point-contacts due to the high level of surface coverage. The NPs were therefore etched using an O_2 plasma process in a Matrix Distributed Electron Cyclotron Resonance (MDECR) reactor. To avoid melting the NPs, the plasma was cycled (15 s ON and 30 s OFF). After the etching process, the 600 nm and 800 nm diameter NP's were found to have diameters of 125±17 nm and 240±13 nm, respectively. A summary of the sample parameters is given in Table 1.

2.3. Forming contacts through the oxide layer

After reducing the size of the NPs and thus decreasing the surface coverage, a thin Aluminum (Al) film was evaporated over the entire surface. After removing the NPs using a toluene bath, a $CHF_3 + Ar$ plasma etching step was used to create the holes in the SiO_2 layer. Finally, the sample was immersed in baths of H_3PO_4 + IPA to etch the Al mask, and underwent an RCA2 cleaning and a 1-min dip in a 1% solution of HF in order to ensure that no metals are left on the sample. Thermal diffusion was then performed in order to locally dope the c-Si through the oxide masking layer, after which the sample again underwent RCA1 and RCA2 cleanings. Each of these cleaning steps was followed by a 20 s dip in HF (2%). Boron diffusion was then performed at 875 °C in an N_2 ambient during 2 h and 30 min in a quartz tube furnace using planar diffusion sources of boron nitride (Saint Gobain Advanced Ceramics) between the wafers to be doped. For the boron diffusion, we followed the same procedure as reported in Ref. [35] including the low temperature oxidation (LTO) that helps in boron rich layer (BRL) removal.

In order to be able to fully characterize the sample surface without the SiO_2 layer, a long, multiple minute dip in a 2% diluted HF solution was performed, until the surface became completely hydrophobic. Just before C-AFM measurements, a further 1 min 1% HF dip was done to remove any native oxide that would have formed.

2.4. Nanoscale characterization

The samples were observed using a Hitachi S-4800 scanning electron microscope (SEM). This microscope is equipped with two detectors: the upper detector, which detects only secondary electrons (SE), and the lower detector, which detects mainly back-scattered electrons (BSE). A mixed detection mode (SE + BSE, using both detectors) can be used to obtain topological information, as can the SE-only mode (but only at high beam voltages). Furthermore, the SE-only mode at low voltages can be used to observe localized doping, since the contrast in this mode is sensitive to the doping type of the material [36–41].

The samples were also characterized using a Digital Instruments Nanoscope IIIa Multimode Atomic Force Microscope (AFM) using a C-AFM electrical extension named "Resiscope", which allows one to get an electrical map in parallel to the topography when measuring the current flowing through the tip [42,43]. For these measurements a bias voltage is applied between the tip and the back side of the sample. In addition, contact current-voltage (I–V) measurements at a desired point on the sample are also possible. It should be noted that the AFM deflection system uses a laser at a wavelength of 670 nm. Finally, for this study the AFM tips employed were highly p-doped polycrystalline diamond (3–5 mΩ cm, CDT-FMR) with a "macroscopic" radius in the range of 100 nm and a spring constant around 3 N/m for the batch used. Because of their polycrystalline structure, the apex of these tips are characterized by microscopic single diamond grains providing an electrical tip radius of 10 nm. The estimated force applied for scanning measurements where around 100 nN and in the range of 100–500 nN for point contact current-voltage (I–V) measurements.

Table 1
Sample properties before diffusion step.

Sample ID	Wafer resistivity (Ω cm)	Thickness of SiO_2 passivation layer	Initial NP diameter	NP diameter after etching
A	1	120 nm	600 nm	125 nm
B	2.2	240 nm	800 nm	240 nm

3. Results and discussion

3.1. Scanning electron microscopy

Fig. 1 shows SEM images of Sample A acquired at various points of the process used to form the doped nanojunctions, as described above. Similar images for Sample B are provided in the Supplementary Material. All of these images were taken using the SE-only mode at high voltages.

Fig. 1a is a SEM image of the c-Si covered with oxide and the 125 nm etched NPs, and Fig. 1b shows the sample after Al evaporation and NP removal (after which holes of 200 ± 18 nm were formed in the Al). Fig. 1c–d shows the holes formed in the oxide layer after plasma etching and Al removal, and after which holes with diameters around 220 ±30nm remain, giving an f_c of around 10%. Fig. 1e–f shows the sample after diffusion and LTO. Around 30 nm of thermal oxide remained on the sample from the original oxide layer of 120 nm, this reduced thickness being due to the HF steps done at various points in the process, and the oxide etching that occurs during the diffusion.

Fig. 1g–h shows the sample after SiO_2 removal. From the top view image, it can be seen that the areas around the holes appear brighter than both the holes and the surrounding areas. In addition, it can be seen that there are craters formed in the Si. From the SEM cross sectional image, it can be seen that the depth of these craters is around 35 nm and that they have a "dinner plate" shape. This particular shape is due to the process of boron glass formation during the doping process and etching inside the hole.

The areas shown in cross section in Fig. 1f–h were examined more closely. SEM images were acquired at 1 kV using either SE-only mode or the mixed mode, and are shown in Fig. 2. The equivalent images for Sample B are provided in the Supplementary Material.

Fig. 2a–b shows the same location on Sample A after the LTO step, but Fig. 2a is acquired in SE-only mode, whereas Fig. 2b was acquired in mixed mode. Fig. 2c (SE-only) and 2d (mixed) were acquired after SiO_2 removal. The bright areas under the holes appear only when the SE-only mode is used, while the mixed mode gives only topographical information.

In previous reports, a greater brightness was observed for p-type regions compared to n-type regions when SEM images were obtained using "SE-only" detectors and at low beam voltages [36–41]. This observation is therefore consistent with the areas below the openings being doped p-type.

3.2. Conductive probe atomic force microscopy analysis

C-AFM measurements were then performed on Sample A, after submitting the sample to an additional HF dip. Fig. 3a and b presents the topography and the local resistance maps, respectively. The latter was obtained by applying first a voltage of −1 V (first half of the top of the image) and then switching to +1 V (second half). The equivalent image for Sample B measured at +1 V is provided in the Supplementary Material. The resulting local resistance map is obtained through Ohm's law by dividing the applied voltage by the measured local current through the AFM tip. Note that for this mapping measurement, the voltage was applied to the n-type c-Si substrate through an ohmic contact to the bulk on the rear surface of the sample.

Fig. 3c and d shows examples of profiles taken at the upper (black dotted lines) and lower (black dashed lines) part of the image. The topography profiles confirm the previous cross-sectional SEM images, and reveal craters with depths varying in the range 20–40 nm. The resistance profiles taken along the same locations show resistance values inside the craters in the range 10^7–10^9 Ω for −1 V (upper part) and 10^6–10^7 Ω for +1 V (lower part). The difference in resistance between these two voltages suggests a rectifying behavior, whose origin can be explained by the local p-type doped region inside the craters forming a p-n junction with the n-type c-Si substrate. Similar behavior can also be observed in the areas surrounding the craters; however, in that case the rectifying junction is between the boron-doped diamond of the AFM tip and the n-type c-Si substrate. Note, that the homogeneous colors observed in the electrical image suggest that the doping is rather uniform in the craters and that the variations observed in some profiles may result from a variation in the electrical contact area.

To illustrate these points, Fig. 4 displays an example of a current-voltage (I–V) measurement performed inside a crater (filled black circles) and around the craters (red line). The absolute value of the current is used to allow its representation on a semi-log scale. For the black curve, measured within the crater, a typical diode-like rectification behavior is indeed observed, in addition to an unexpected zero-crossing in current occurring for a negative applied voltage. The I–V characteristic obtained outside the crater shows an asymmetric behavior, also with large variations of the electrical current level depending on the applied voltage. These two point contact I–V curves clarify the previous local resistance mapping (Fig. 3b) and specifically the differences between the reverse and forward operation regimes. In addition, these local I–V characterizations further reveal the presence of a PV ef-

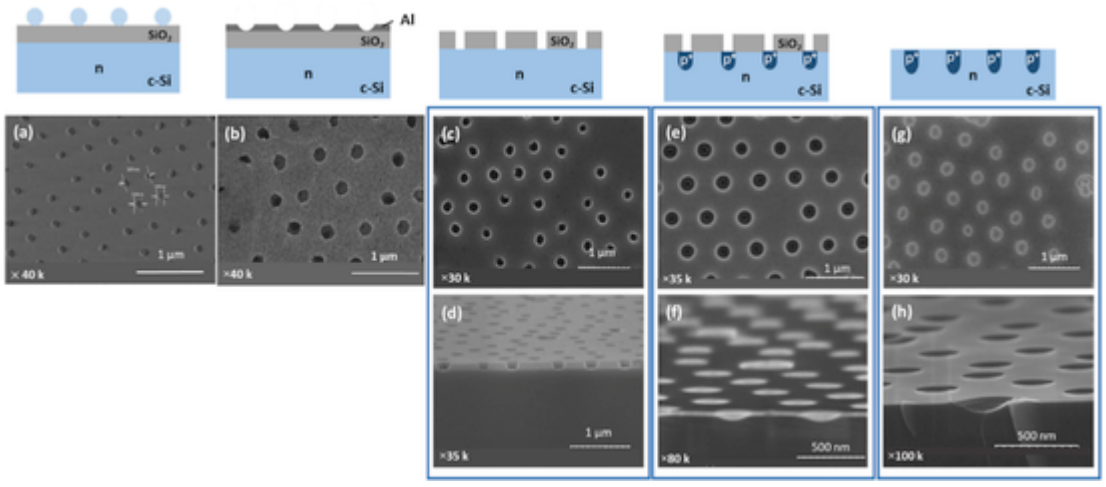

Fig. 1. SEM images of c-Si sample A at various points of localized diffusion process. (a) Oxide covered with NPs, (b) holes formed in the Al covering the oxide layer, (c) top and (d) tilted view of holes formed in the oxide before diffusion. Also shown are (e) top and (f) tilted view of oxide with holes after diffusion and LTO steps, as well as (g) top and (h) tilted view of surface after oxide removal.

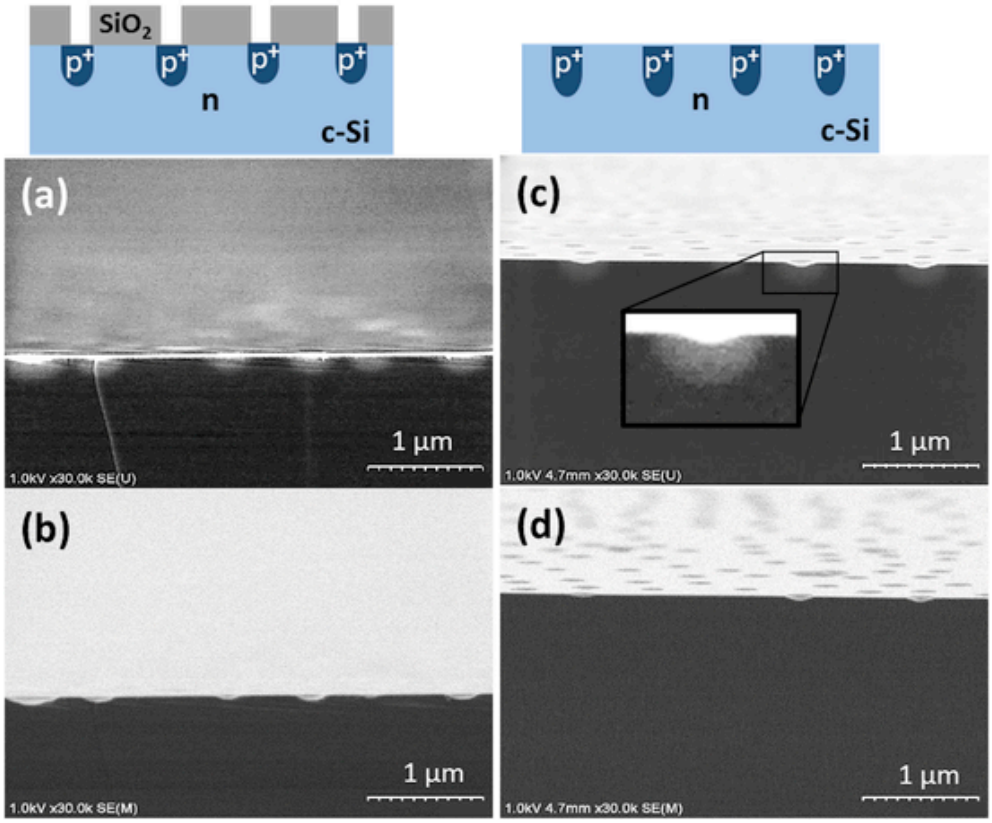

Fig. 2. SEM cross sectional images of localized dopant diffusion areas in c-Si (contrast enhanced). Sample A after the LTO step, taken in (a) SE-only mode, and (b) mixed mode. The same sample is shown after SiO_2 removal, images acquired in (c) SE-only mode, and (d) mixed mode. Inset of (c): contrast enhanced zoom of area under hole in oxide.

fect when performed inside the crater, with a short-circuit current (I_{SC}) around 0.1 µA and an open-circuit voltage (V_{OC}) of 500–600 mV.

The preceding results underline an important insight: not only is it unambiguously confirmed that the craters are indeed locally p-doped areas forming p-n nanojunctions with the n-type c-Si, but that a photovoltaic effect is also present. The diameter of the red (670 nm) laser beam involved in the optical beam deflection system is large compared to the size of the AFM cantilever and the light is also scattered by the cantilever edges. This implies that mostly areas quite far (microns away) from the tip are strongly illuminated. Despite the well-known shadowing effect by AFM cantilevers [44], the light is here absorbed by the c-Si absorber and the photogenerated e-h pairs are able to diffuse toward their corresponding collection sites. Real dark conditions are not achievable due to the feedback loop which is required during the scanning for the stabilization of the tip setpoint in this AFM setup [45]. Consequently, an additional experiment was done to minimize the effect of the laser by changing the excitation wavelength to the infrared (λ = 1300 nm) beyond the optical bandgap of the c-Si. The dramatic decrease in the measured Isc and V_{OC} confirmed that photogeneration is mainly caused by the red laser (these results are included in the Supplementary Material).

Taking advantage of the unexpected light source, we have characterized and compared the different samples and especially the PV characteristics extracted through the locally p-doped craters, or nanojunctions. Fig. 5 displays the I–V curves acquired for both Sample A, which has smaller junction areas spaced closer together (230 nm diameter junctions spaced at least 600 nm apart), and Sample B (250 nm diameter junctions spaced at least 800 nm apart). The graphs in the left column are plotted on a semi-log scale and show several examples of I–V measurements obtained within the nanojunctions (empty symbols) and outside the nanojunctions (full and dashed grey lines). The graphs on the right are linear scale replots of the I–V curves obtained inside the nanojunctions. The semi-log plots clearly demonstrate the presence of the PV effect for both samples, embodied by the presence of a V_{OC}, which is similar for both samples, and an I_{SC}. An s-shape behavior indicating a non-ohmic contact was observed for both sample A (Fig. 5b, green hexagons) and B (Fig. 5d, pink rectangles); however, it has been minimized by simply increasing the applied force between the AFM tip and the nanojunction from 100 nN to 500 nN (as shown), producing an ohmic contact between the tip and the p-type area, and giving the monotonic curves expected for a PV device (red circles in both figures). Note that in these figures, the I–V measurements were acquired while increasing the applied force, but were collected at the same location.

The best I–V characteristics measured inside the nanojunctions for the two samples are compared on the same linear scale in Fig. 6. The photovoltaic parameters extractable from these curves are presented in Table 2. The samples show a similar V_{OC} (within the precision of the measurement) and a similar series resistance is observed for both samples. However, Sample A shows both a larger I_{SC} and a smaller shunt resistance (a greater slope around I_{SC}). The higher I_{SC} for Sample A is counterintuitive, as the nanojunction areas is slightly smaller. This result can be explained by a combination of the collection area being much larger than the nanojunction itself, along with a slightly different alignment of the laser that introduces some scatter in the results. Although the AFM tip cantilever will shadow the area around the nanojunction under test, notice that the high quality of the c-Si substrate along with the H-termination of the surface after the final HF dip (or a thin layer of native oxide) can lead to relatively high effective lifetimes. This low recombination permits the collection of holes photogenerated in the n-type c-Si bulk several microns away from the nanojunction under test. Furthermore, one should consider that a total I_{SC} of ~0.5 µA corresponds to a total laser power of ~1 µW at 670 nm, so we are only collecting a tiny fraction of the incident laser power, the rest being re-

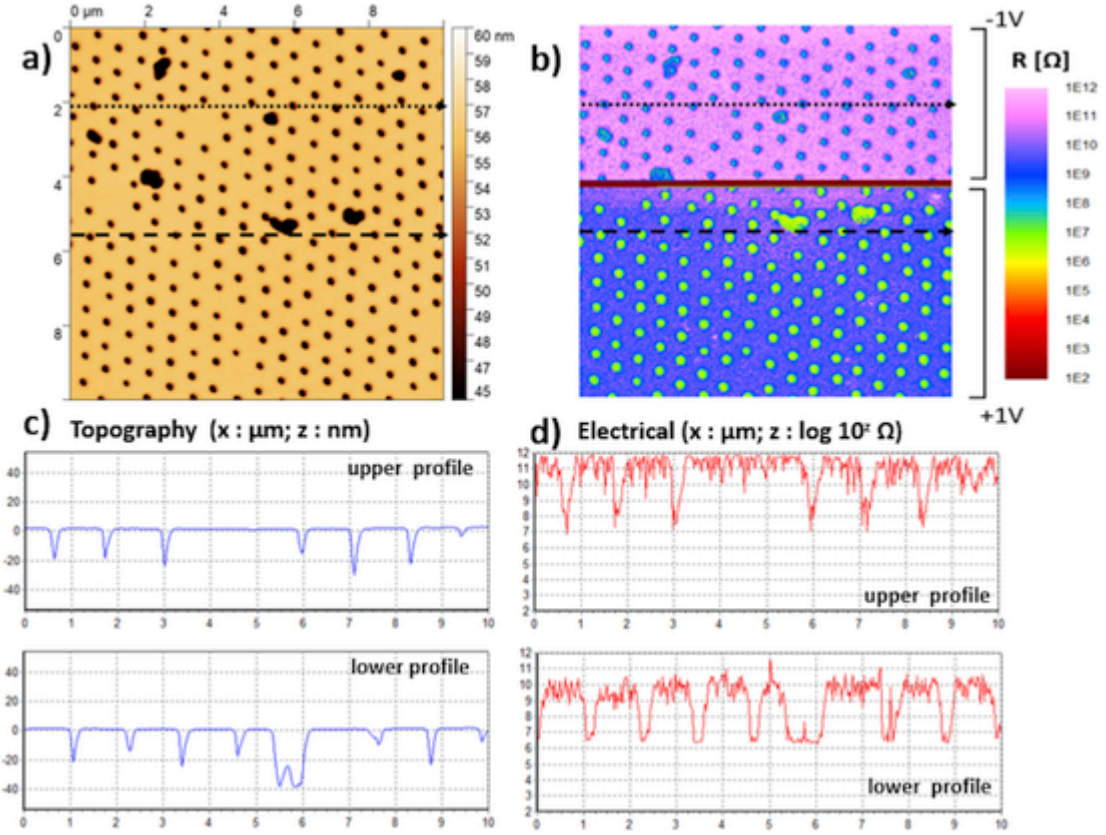

Fig. 3. C-AFM measurements of Sample A. a) Topography image, and b) local resistance mapping while applying a bias of −1 V (upper part) and +1 V (lower part), c) topography and d) local resistance profiles corresponding to the black dotted line (upper profile) and the black dashed line (lower profile).

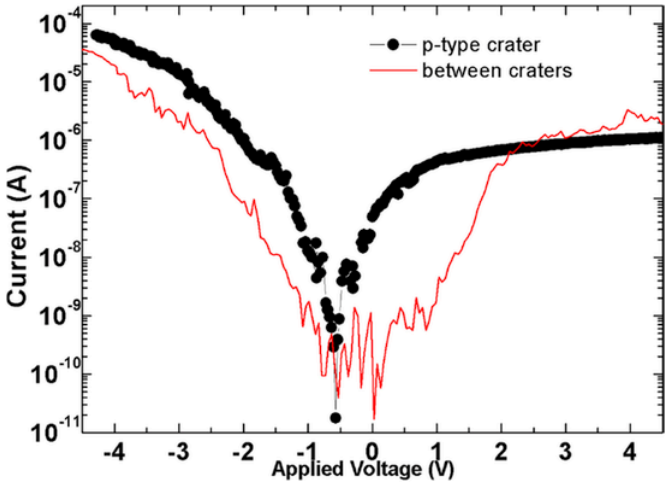

Fig. 4. Example of C-AFM I–V measurement. Measurement was performed on Sample A inside a crater (black filled circle) and around the craters (red full line). Absolute value of current is shown. (For interpretation of the references to color in this figure legend, the reader is referred to the Web version of this article.)

flected by the cantilever, or producing photocarriers that recombine before collection.

As well, due to the configuration of the measurement, the significance of the shunt resistance may not be straightforward. Two possible explanations are real shunting effects related to the perimeter (which can have a very strong impact in such small nanojunctions), or photocurrent collected through a much more resistive pathway (such as an inversion layer at the surface) giving the appearance of a shunt.

Although interpretation of the details of the I–V curve remains difficult, the clear appearance of a VOC and an ISC for both samples shows without a doubt that photovoltaic nanojunctions have been formed in both samples.

4. Conclusions

We have demonstrated the formation of p-doped, nanoscale junctions in n-doped crystalline silicon wafers through the observation of a local photovoltaic effect. The necessary photoexcitation is provided by the red laser used to determine tip position for conductive-probe atomic force microscopy (C-AFM) measurements. By acquiring local I–V curves rather than pseudo-resistance mapping, clear evidence of photovoltaic behavior due to the formation of a nanojunction could be observed, which was consistent with cross-sectional SEM images using low beam voltages and the secondary-electron-only detector, wherein a brightness contrast consistent with a localized p-type doping could be observed. From a purely prospective point of view, acquiring I–V measurement in dark conditions and/or under a well-defined and calibrated illumination would be a major advantage for the electrical characterization of these nanojunctions, and notably for statistical analyses. Such studies would impose that the laser required for tip alignment no longer interacts with the sample (either by being turned off, diverted, or having a longer wavelength), and that the illumination is not shadowed by the AFM tip (possibly by being injected from the other side of the sample).

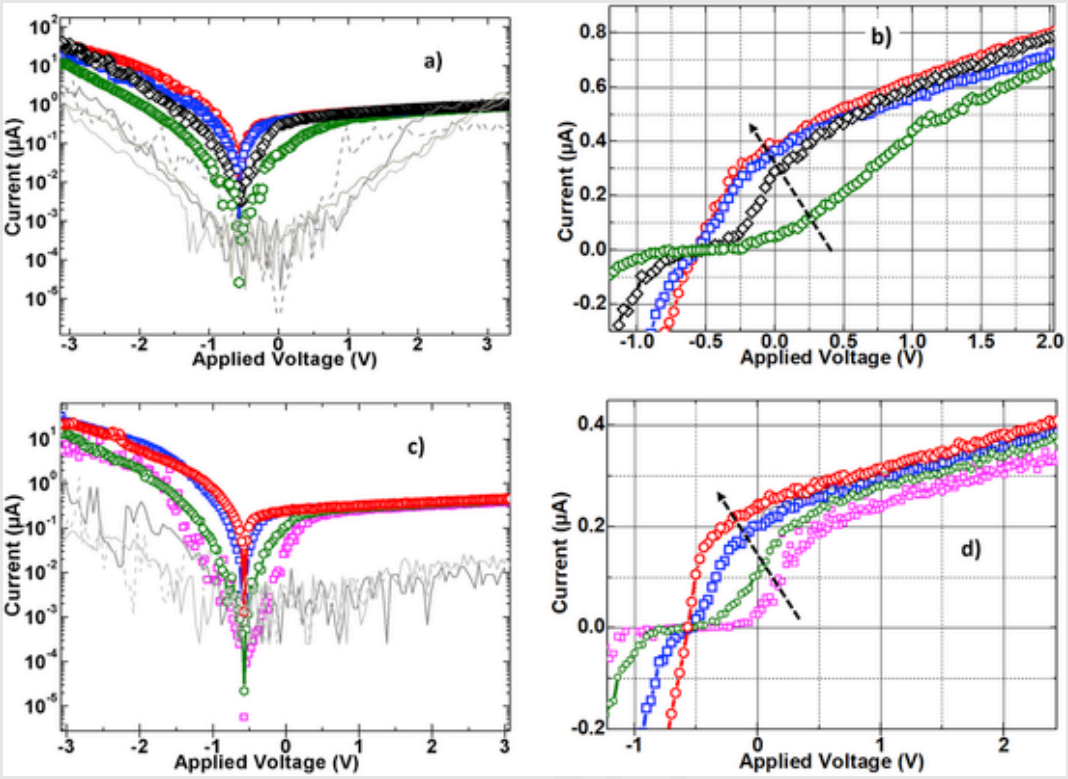

Fig. 5. Local I–V curves measured using C-AFM. Curves are measured on Sample A (figs a) and b)), and Sample B (figs c) and d)). Left column a) and c) illustrates the I–V curves on a semi-log scale performed inside the nanojunctions (empty symbols) and outside the nanojunctions (grey full and dashed lines). Right column (b), and d)) replots the I–V measurements obtained inside the nanojunctions (empty symbols) on a linear scale. Improved characteristics are due to increased tip force from 100 nN to 500 nN, as indicated by arrow.

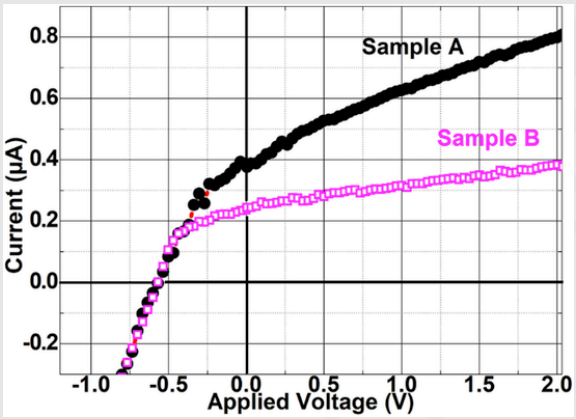

Fig. 6. Comparison of photovoltaic effect in both samples. I–V curves measured by C-AFM measured within the p-type nanojunctions for Samples A and B.

Table 2
PV parameters.

Sample ID	Contact Area (μm^2)	Thickness of SiO_2 passivation layer	V_{OC} (V)	I_{SC}
A	0.04	120 nm	0.57	363 nA
B	0.05	240 nm	0.57	236 nA

[1] A W Blakers, A Wang, A M Milne, J Zhao, M A Green, 22.8% efficient silicon solar cell, Appl. Phys. Lett. 55 (1989) 1363–1365, doi:10.1063/1.101596.
[2] M A Green, The path to 25% silicon solar cell efficiency: history of silicon cell evolution, Prog. Photovoltaics Res. Appl. 17 (2009) 183–189, doi:10.1002/pip.892.
[3] S Philipps, F Ise, W Warmuth, Photovoltaics Report - Fraunhofer, ISE, 2017.
[4] A Blakers, Development of the PERC solar cell, IEEE J. Photovoltaics 9 (2019) 629–635, doi:10.1109/JPHOTOV.2019.2899460.
[5] T Dullweber, J Schmidt, Industrial silicon solar cells applying the passivated emitter and rear cell (PERC) concept-A review, IEEE J. Photovoltaics 6 (2016) 1366–1381, doi:10.1109/JPHOTOV.2016.2571627.

[6] J Zhao, A Wang, M A Green, Series resistance caused by the localized rear contact in high efficiency silicon solar cells, Sol. Energy Mater. Sol. Cells 32 (1994) 89–94, doi:10.1016/0927-0248(94)90258-5.
[7] K R Catchpole, A W Blakers, Modelling the PERC structure for industrial quality silicon, Sol. Energy Mater. Sol. Cells 73 (2002) 189–202, doi:10.1016/S0927-0248(01)00124-6.
[8] R Khoury, I Martín, C López, G Jin, J M López-González, L Zeyu, P Bulkin, E V Johnson, R Alcubilla, Partially Contacted Surfaces with Contact Size in the 1 μm Range for C-Si PERC Solar Cells, IEEE PVSC, 2017.
[9] C H Hsu, C H Yang, Y H Wang, C W Huang, S Y Lien, C Y Kung, J C Lou, Low cost local contact opening by using polystyrene spheres spin-coating method for PERC solar cells, Materials (Basel) 9 (2016), doi:10.3390/ma9070549.
[10] S J O'Shea, R M Atta, M E Welland, Characterization of tips for conducting atomic force microscopy, Rev. Sci. Instrum. 66 (1995) 2508–2512.
[11] M A Lantz, S J O'Shea, M E Weiland, Characterization of tips for conducting atomic force microscopy in ultrahigh vacuum, Rev. Sci. Instrum. 69 (1998) 1757–1764, doi:10.1063/1.1148838.
[12] F Houzé, R Meyer, O Schneegans, L Boyer, Imaging the local electrical properties of metal surfaces by atomic force microscopy with conducting probes, Appl. Phys. Lett. 69 (1996) 1975–1977, doi:10.1063/1.117179.
[13] J Planès, F Houzé, P Chrétien, O Schneegans, Conducting probe atomic force microscopy applied to organic conducting blends, Appl. Phys. Lett. 79 (2001) 2993–2995, doi:10.1063/1.1413717.
[14] U Celano, Electrical Atomic Force Microscopy for Nanoelectronics, Springer International Publishing, 2019, doi:10.1007/978-3-030-15612-1.
[15] D L Klein, P L McEuen, Conducting atomic force microscopy of alkane layers on graphite, Appl. Phys. Lett. 66 (1995) 2478–2480, doi:10.1063/1.114001.
[16] J Alvarez, F Houzé, J P Kleider, M Y Liao, Y Koide, Electrical characterization of Schottky diodes based on boron doped homoepitaxial diamond films by conducting probe atomic force microscopy, Superlattice. Microst. 40 (2006) 343–349, doi:10.1016/j.spmi.2006.07.027.
[17] J Alvarez, M Boutchich, J P Kleider, T Teraji, Y Koide, Direct observation of the leakage current in epitaxial diamond Schottky barrier devices by conductive-probe atomic force microscopy and Raman imaging, J. Phys. D Appl. Phys. 47 (2014) 355102, doi:10.1088/0022-3727/47/35/355102.
[18] S Tan, Z Tang, X Liang, N A Kotov, Resonance tunneling diode structures on CdTe nanowires made by conductive AFM, Nano Lett. 4 (2004) 1637–1641, doi:10.1021/nl0492077.
[19] C Renard, T Molière, N Cherkashin, J Alvarez, L Vincent, A Jaffré, G Hallais, J P Connolly, D Mencaraglia, D Bouchier, High current density GaAs/Si rectifying heterojunction by defect free Epitaxial Lateral overgrowth on Tunnel Oxide from nano-seed, Sci. Rep. 6 (2016) 25328, doi:10.1038/srep25328.
[20] M A Rafiq, Carrier transport mechanisms in semiconductor nanostructures and devices, J. Semiconduct. 39 (2018) 61002, doi:10.1088/1674-4926/39/6/061002.
[21] O G Reid, K Munechika, D S Ginger, Space charge limited current measurements on conjugated polymer films using conductive atomic force microscopy, Nano Lett. 8 (2008) 1602–1609, doi:10.1021/nl080155l.
[22] J L Luria, N Hoepker, R Bruce, A R Jacobs, C Groves, J A Marohn, Spectroscopic imaging of photopotentials and photoinduced potential fluctuations in a bulk heterojunction solar cell film, ACS Nano 6 (2012) 9392–9401, doi:10.1021/nn300941f.
[23] H Dai, E W Wong, C M Lieber, Probing electrical transport in nanomaterials: conductivity of individual carbon nanotubes, 80-. Science (1996) 272 523 LP – 526, doi:10.1126/science.272.5261.523.
[24] J H He, S Te Ho, T B Wu, L J Chen, Z L Wang, Electrical and photoelectrical performances of nano-photodiode based on ZnO nanowires, Chem. Phys. Lett. 435 (2007) 119–122, doi:10.1016/j.cplett.2006.12.061.
[25] C de Melo, M Jullien, J Ghanbaja, F Montaigne, J-F Pierson, F Soldera, F Rigoni, N Almqvist, A Vomiero, F Mücklich, D Horwat, Local structure and point-defect-dependent area-selective atomic layer deposition approach for facile synthesis of p-Cu2O/n-ZnO segmented nanojunctions, ACS Appl. Mater. Interfaces 10 (2018) 37671–37678, doi:10.1021/acsami.8b12584.
[26] D Kanematsu, S Yata, A Terakawa, M Tanaka, M Konagai, Photovoltaic properties of axial-junction silicon nanowire solar cells with integrated arrays, Jpn. J. Appl. Phys. 54 (2015), doi:10.7567/JJAP.54.08KA09.
[27] H Li, X X Liu, Y S Lin, B Yang, Z M Du, Enhanced electrical properties at boundaries including twin boundaries of polycrystalline CdTe thin-film solar cells, Phys. Chem. Chem. Phys. 17 (2015) 11150–11155, doi:10.1039/C5CP00564G.
[28] W Li, S R Cohen, K Gartsman, D Cahen, Ga composition dictates macroscopic photovoltaic and nanoscopic electrical characteristics of Cu(in $_{1-X}$Ga$_X$)Se $_2$ thin films via grain-boundary-type inversion, IEEE J. Photovoltaics 2 (2012) 191–195, doi:10.1109/JPHOTOV.2012.2184266.
[29] D Mikulik, M Ricci, G Tutuncuoglu, F Matteini, J Vukajlovic, N Vulic, E Alarcon-Llado, A Fontcuberta i Morral, Conductive-probe atomic force microscopy as a characterization tool for nanowire-based solar cells, Nano Energy 41 (2017) 566–572, doi:10.1016/j.nanoen.2017.10.016.
[30] J Alvarez, C Marchat, A Morisset, L Dai, J-P Kleider, R Cabal, P R i Cabarrocas, Electrical scanning probe microscopy approaches to investigate solar cell junctions and devices, Proc. SPIE (2020), doi:10.1117/12.2540422.
[31] P Narchi, J Alvarez, P Chrétien, G Picardi, R Cariou, M Foldyna, P Prod'homme, J-P Kleider, P R i Cabarrocas, Cross-sectional investigations on epitaxial silicon solar cells by kelvin and conducting probe atomic force microscopy: effect of illumination, Nanoscale Res. Lett. 11 (2016) 55, doi:10.1186/s11671-016-1268-1.
[32] O A Maslova, J Alvarez, E V Gushina, W Favre, M E Gueunier-Farret, A S Gudovskikh, A V Ankudinov, E I Terukov, J P Kleider, Observation by conductive-probe atomic force microscopy of strongly inverted surface layers at the hydrogenated amorphous silicon/crystalline silicon heterojunctions, Appl. Phys. Lett. 97 (2010) 252110, doi:10.1063/1.3525166.
[33] Y J Zhang, Synthesis of One-Dimensional Silicon Nanopillar Arrays Assisted by Polystyrene Spheres, City University of Hong Kong, 2012.
[34] J R Oh, J H Moon, S Yoon, C R Park, Y R Do, Fabrication of wafer-scale polystyrene photonic crystal multilayers via the layer-by-layer scooping transfer technique, J. Mater. Chem. 21 (2011) 14167, doi:10.1039/c1jm11122a.
[35] G Masmitja, P Ortega, G Lopez, E Calle, M Garcia, I Martin, A Orpella, C Voz, R Alcubilla, IBC c-Si(n) solar cells based on laser doping processing for selective emitter and base contact formation, Energy Procedia 92 (2016) 956–961.
[36] D D Perovic, M R Castell, A Howie, C Lavoie, T Tiedje, J S W Cole, Field-emission SEM imaging of compositional and doping layer semiconductor superlattices, Ultramicroscopy 58 (1995) 104–113, doi:10.1016/0304-3991(94)00183-N.
[37] T Sekiguchi, T Kimura, H Iwai, SEM observation of p-n junction in semiconductors using fountain secondary electron detector, Superlattice. Microst. 99 (2016) 165–168, doi:10.1016/j.spmi.2016.03.020.
[38] S L Elliott, R F Broom, C J Humphreys, Dopant profiling with the scanning electron microscope - a study of Si, J. Appl. Phys. 91 (2002) 9116–9122, doi:10.1063/1.1476968.
[39] R Turan, D D Perovic, D C Houghton, Mapping electrically active dopant profiles by field-emission scanning electron microscopy, Appl. Phys. Lett. 69 (1996) 1593–1595, doi:10.1063/1.117041.
[40] M R Castell, T W Simpson, I V Mitchell, D D Perovic, J-M Baribeau, Deactivation and diffusion of boron in ion-implanted silicon studied by secondary electron imaging, Appl. Phys. Lett. 74 (1999) 2304–2306, doi:10.1063/1.123832.
[41] C P Sealy, M R Castell, P R Wilshaw, Mechanism for secondary electron dopant contrast in the SEM, J. Electron Microsc. (Tokyo) 49 (2000) 311–321, doi:10.1093/oxfordjournals.jmicro.a023811.
[42] M Stangoni, M Ciappa, W Fichtner, Assessment of the analytical capabilities of scanning capacitance and scanning spreading resistance microscopy applied to semiconductor devices, Microelectron. Reliab. 45 (2005) 1532–1537, doi:10.1016/j.microrel.2005.07.058.
[43] N Duhayon, P Eyben, M Fouchier, T Clarysse, W Vandervorst, D Álvarez, S Schoemann, M Ciappa, M Stangoni, W Fichtner, P Formanek, M Kittler, V Raineri, F Giannazzo, D Goghero, Y Rosenwaks, R Shikler, S Saraf, S Sadewasser, N Barreau, T Glatzel, M Verheijen, S A M Mentink, M Von Sprekelsen, T Maltezopoulos, R Wiesendanger, L Hellemans, Assessing the performance of two-dimensional dopant profiling techniques, J. Vac. Sci. Technol. B 22 (2004) 385, doi:10.1116/1.1638775.
[44] C Marchat, L Dai, J Alvarez, S Le Gall, J-P Kleider, S Misra, P Roca i Cabarrocas, Local VOC measurements by kelvin probe force microscopy applied on P-I-N radial junction Si nanowires, Nanoscale Res. Lett. 14 (2019) 398, doi:10.1186/s11671-019-3230-5.
[45] M Ledinsky, A Fejfar, A Vetushka, J Stuchlik, B Rezek, J Kocka, Local photoconductivity of microcrystalline silicon thin films measured by conductive atomic force microscopy, Phys. Status Solidi Rapid Res. Lett. 5 (2011) 373–375, doi:10.1002/pssr.201105413.